

NNT : \*\*\*

n°LAL : \*\*\*

Thèse de doctorat

# Search of the $0\nu\beta\beta$ decay with the SuperNEMO demonstrator

Thèse de doctorat de l'Université Paris-Saclay  
préparée à l'Université Paris Saclay au sein du Laboratoire Irène-Joliot Curie  
(anciennement Laboratoire de l'Accélérateur Linéaire)

École doctorale n°576 Particles, Hadrons, Energy, Nuclei, Instrumentation,  
Imaging, Cosmos et Simulation (PHENIICS)  
Spécialité de doctorat : Physique des particules

Thèse présentée et soutenue à Orsay, le \*\*\*, par

**CLOÉ GIRARD-CARILLO**

Composition du Jury :

\*\*\*

\*\*\*

Président

\*\*\*

\*\*\*

Rapporteur

\*\*\*

\*\*\*

Rapporteur

Christine Marquet  
CENBG - Bordeaux-Gradignan

Examineur

\*\*\*

\*\*\*

Examineur

\*\*\*

\*\*\*

Examineur

Laurent Simard  
LAL - Orsay

Directeur de thèse

Mathieu Bongrand  
LAL - Orsay

Co-directeur de thèse



---

# Contents

<b>Contents</b>	<b>3</b>
<b>Introduction</b>	<b>7</b>
<b>1 Phenomenology of particle physics</b>	<b>9</b>
1.1 The Standard Model of particle physics . . . . .	9
1.1.1 Bosons . . . . .	9
1.1.2 Fermions . . . . .	9
1.1.3 $2\nu\beta\beta$ decay . . . . .	9
1.1.4 Where the Standard Model ends . . . . .	9
1.2 Going beyond the Standard Model with neutrinos . . . . .	9
1.2.1 Neutrino flavors and oscillations . . . . .	9
1.2.2 Neutrino masses and nature . . . . .	9
1.2.3 Other searches beyond the Standard Model with neutrinos . . . . .	9
<b>2 <math>0\nu\beta\beta</math> experiment status</b>	<b>11</b>
2.1 Experimental design criteria . . . . .	11
2.1.1 Aspects of the nuclear matrix elements . . . . .	12
2.1.2 Quenching . . . . .	12
2.2 $0\nu\beta\beta$ direct search experiments . . . . .	12
2.2.1 Semiconductors . . . . .	12
2.2.2 Bolometers . . . . .	13
2.2.3 Time projection chambers . . . . .	13
2.2.4 Scintillators . . . . .	16
2.2.5 Tracking calorimeters . . . . .	16
<b>3 The SuperNemo demonstrator</b>	<b>17</b>
3.1 The SuperNemo demonstrator . . . . .	17
3.1.1 Comparison with Nemo3 experiment . . . . .	17
3.1.2 Experimental design . . . . .	17
3.1.3 Sources . . . . .	17
3.1.4 Tracker . . . . .	17
3.1.5 Calorimeter . . . . .	17

3.1.5.1	Scintillator . . . . .	17
3.1.5.2	Photomultiplier . . . . .	17
3.1.6	Calibration systems . . . . .	17
3.1.7	Control Monitoring system . . . . .	17
3.1.8	Electronics . . . . .	17
3.2	The background of SuperNEMO . . . . .	17
3.2.1	Internal background . . . . .	17
3.2.2	External background . . . . .	18
3.2.3	Background specifications . . . . .	18
3.2.4	Measured demonstrator background levels . . . . .	18
3.3	Magnetic field . . . . .	18
3.4	The SuperNemo software . . . . .	18
3.4.1	Simulation . . . . .	18
3.4.2	Reconstruction . . . . .	18
<b>4</b>	<b>Analysis tools</b>	<b>19</b>
4.1	Internal and external probabilities . . . . .	19
4.1.1	Internal probability . . . . .	19
4.2	Simulations . . . . .	20
4.2.1	Modifications of simulation software . . . . .	20
4.2.2	Internal background simulations . . . . .	20
4.2.3	$0\nu\beta\beta$ simulations . . . . .	20
<b>5</b>	<b>Time difference</b>	<b>21</b>
5.1	Principle and goal . . . . .	21
5.1.1	Internal conversion . . . . .	21
5.2	Analysis . . . . .	22
5.2.1	Topological cuts . . . . .	22
5.2.2	Exponentially modified Gaussian . . . . .	22
5.2.3	Results . . . . .	22
5.3	Conclusion . . . . .	22
<b>6</b>	<b>Sensitivity of the SuperNEMO demonstrator to the <math>0\nu\beta\beta</math></b>	<b>25</b>
6.1	Signal and background simulations . . . . .	25
6.1.1	The $0\nu\beta\beta$ signal . . . . .	26
6.1.2	Inside detector backgrounds . . . . .	27
6.1.2.1	Internal backgrounds . . . . .	27
6.1.2.2	Tracker contamination by natural isotopes . . . . .	27
6.1.3	Outside detector backgrounds . . . . .	28
6.2	Optimisation of event selection . . . . .	28
6.3	Expected number of background events and optimisation of the region of interest . . . . .	30
6.4	The 25 Gauss magnetic field . . . . .	33
6.4.1	Influence of the magnetic field on optical modules and reconstruction efficiency . . . . .	33
6.4.2	Simulations of the magnetic field inside the demonstrator and reconstructed track fit . . . . .	33

6.5	Demonstrator sensitivity to the $0\nu\beta\beta$ decay . . . . .	34
6.5.1	Influence of the contamination levels . . . . .	35
6.5.2	Influence of the magnetic field . . . . .	36
6.6	Final detector sensitivity . . . . .	36
6.7	Other isotopes . . . . .	36
6.8	Conclusion . . . . .	37
<b>7</b>	<b>Detector commissioning</b>	<b>39</b>
7.1	Reflectometry analysis . . . . .	39
7.1.1	Goal of the reflectometry analysis . . . . .	39
7.1.2	Pulse timing: controlling cable lengths . . . . .	40
7.1.3	Signal attenuation . . . . .	45
7.1.4	Pulse shape analysis . . . . .	47
7.1.5	Comparison with $^{60}\text{Co}$ . . . . .	47
7.1.6	Conclusion . . . . .	47
7.2	Calibrating the electronic boards . . . . .	47
7.2.1	Principle . . . . .	47
7.2.2	Measuring the time offset of front end boards . . . . .	47
7.2.3	Results . . . . .	47
7.3	Energy calibration of optical modules . . . . .	47
7.4	Baseline studies . . . . .	47
7.5	Light Injection System . . . . .	47
<b>8</b>	<b>Characterisation of the calorimeter time resolution</b>	<b>49</b>
8.1	Interaction of particles in the SuperNEMO scintillators . . . . .	50
8.1.1	Interaction of electrons . . . . .	50
8.1.2	Interaction of photons . . . . .	50
8.2	Measurement of the time resolution with a $^{60}\text{Co}$ source . . . . .	51
8.2.1	Description of Cobalt 60 nucleus . . . . .	52
8.2.2	Time response of optical modules . . . . .	52
8.2.3	Final experimental design . . . . .	55
8.2.4	Signal events selection . . . . .	57
8.2.5	Background estimation . . . . .	59
8.2.6	Detector efficiency . . . . .	63
8.2.7	Determination of the individual timing resolution of each optical module . . . . .	64
8.2.8	Conclusion . . . . .	68
8.3	The Light Injection System . . . . .	68
8.3.1	Light injection system commissioning . . . . .	69
8.3.2	Time resolution of optical modules . . . . .	69
	<b>Conclusion</b>	<b>71</b>
	<b>Bibliography</b>	<b>73</b>



## Sensitivity of the SuperNEMO demonstrator to the $0\nu\beta\beta$

In this chapter, we present a study aiming to evaluate the SuperNEMO's sensitivity to the  $0\nu\beta\beta$  decay, and the corresponding effective neutrino masses. Studies of this kind have already been conducted, and the final detector is expected to exclude half-lives up to  $1.2 \times 10^{26}$  y (90% CL), with an exposure of 500 kg.y for the  $^{82}\text{Se}$ <sup>1</sup> [7]. In 2015 began the demonstrator installation at the Laboratoire Souterrain de Modane, aiming to assess the feasibility of such a large scale detector based on the NEMO-3 technology. With an exposure of 17.5 kg.y, the demonstrator could reach a sensitivity on the  $0\nu\beta\beta$  process of  $5.3 \times 10^{24}$  y (90% CL) [8].

At the time of the current analysis, the coil, which is supposed to deliver a magnetic field inside the detector, was not yet installed on the demonstrator. We aim to explore the impact, on both the demonstrator and final detector sensitivity, of the presence of this magnetic field. The findings of this study will participate in the final decision on the installation of the coil. In a context of investigating the demonstrator and final detector's capabilities, different internal source contamination levels are considered. The topology of interest is the two electrons ( $2e$ ) topology, and we use the total energy sum to discriminate the signal from the background events. Thanks to SuperNEMO tracking capabilities, topological informations are also exploited to improve the sensitivity.

- parler des autres isotopes qu'on voudrait mettre

### 6.1 Signal and background simulations

A full simulation for the demonstrator was performed, in order to determine the upper limit on  $0\nu\beta\beta$  half-life that can be probed with SuperNEMO. In the Tab. 6.1 is summarised the expected number of signal and background events, both for the SuperNEMO demonstrator and final detector. We also present, for each of the process, the amount of simulated events. The figures in the central column represent the total number of disintegrations, without taking into account any

<sup>1</sup>Supposing Selenium-82 decays through the exchange of a light Majorana neutrino.



Type of decay	Expected decays		Simulated decays
	Demonstrator	Final detector	
$0\nu\beta\beta$ ( $T_{1/2}^{0\nu} = 2.5 \cdot 10^{23}$ y)	$3.6 \cdot 10^2$	$1.0 \cdot 10^4$	$1.0 \cdot 10^7$
$2\nu\beta\beta$ ( $T_{1/2}^{2\nu} = 9.39 \times 10^{19}$ y)	$9.5 \cdot 10^5$	$2.7 \cdot 10^7$	$1.0 \cdot 10^7$
$^{208}\text{Tl}$ ( $\mathcal{A}^{\text{Tl}} = 10 \mu\text{Bq/kg}$ )	$5.5 \cdot 10^3$	$1.6 \cdot 10^5$	$1.0 \cdot 10^7$
$^{214}\text{Bi}$ ( $\mathcal{A}^{\text{Bi}} = 2 \mu\text{Bq/kg}$ )	$1.1 \cdot 10^3$	$3.1 \cdot 10^4$	$1.0 \cdot 10^7$
$^{222}\text{Rn}$ ( $\mathcal{A}^{\text{Rn}} = 0.15 \text{ mBq/m}^3$ )	$1.8 \cdot 10^5$	$7.2 \cdot 10^6$	$1.0 \cdot 10^8$

Table 6.1: Expected and simulated decays for different processes, both for the demonstrator (17.5 kg.y) and for the final detector (500 kg.y), assuming target background activities are reached:  $\mathcal{A}^{\text{Tl}} = 10 \mu\text{Bq/kg}$ ,  $\mathcal{A}^{\text{Bi}} = 2 \mu\text{Bq/kg}$ ,  $\mathcal{A}^{\text{Rn}} = 0.15 \text{ mBq/m}^3$ . The measured half-life  $T_{1/2}^{2\nu} = 9.39 \times 10^{19}$  y for Selenium-82's  $2\nu\beta\beta$  is taken, and we assume  $T_{1/2}^{0\nu} = 2.5 \times 10^{23}$  y [9].

technique to reject background, and for the total energy window. The amount of expected  $2\nu\beta\beta$  decays is only driven by its  $T_{1/2}^{2\nu}$  value: the higher the half-life of this process, the lower its contribution in the total number of expected background. For Selenium-82 sources, we take the NEMO-3 value  $T_{1/2}^{2\nu} = 9.39 \pm 0.17$  (stat)  $\pm 0.1$  (syst)  $\times 10^{19}$  years [9]. Meanwhile, the expected number for natural isotopes depend on their quantities inside the source foils (for Thallium-208 and Bismuth-214), or on the tracker wires (for Radon-222 decaying in Bismuth-214). It was necessary, during the design of the detector, to set these quantities, to guarantee a high sensitivity to the  $0\nu\beta\beta$  disintegration [11]. These values are given in the table, per disintegration unit per second, for one kg of source material, or for one  $\text{m}^3$  of gas inside the tracker.

Nevertheless, the number of decays presented in the table are expected to be extremely reduced, notably by the application of event selections aimed at maximising the signal over background ratio (Sec. 6.2). Moreover, this effect is augmented by the fact that, for the current sensitivity analysis, we will focus on a narrow energy window, called *region of interest*, whose usefulness will be described in more detail in Sec. 6.3. Therefore, to properly conduct this sensitivity study, it was necessary to simulate a large number of events, so that the signal and backgrounds are correctly represented in the region of interest. Let us now detail the simulations produced as part of this analysis.

### 6.1.1 The $0\nu\beta\beta$ signal

The SuperNEMO detector was designed to search the never-observed  $0\nu\beta\beta$  decay. In the following, we assume the underlying mechanism for this decay is the exchange of a light Majorana neutrino, the so-called mass mechanism (MM), as it is the most natural and widespread mechanism. The hypothetical  $0\nu\beta\beta$  signal would be detected as an excess of events in the region of interest, with respect to the predicted background contamination level. Some  $10^7$   $0\nu\beta\beta$  events were simulated



inside the source foils, using the DECAY0 software [10]. The simulations are normalised assuming a  $T_{1/2}^{0\nu} = 2.5 \cdot 10^{23}$  y half-life [9].



## 6.1.2 Inside detector backgrounds

In addition with the  $0\nu\beta\beta$  decay, we simulated different types of backgrounds, that could mimic the searched signal.

### 6.1.2.1 Internal backgrounds

The so-called *internal backgrounds* stand for decays occurring inside the source foils, presenting the same signature as the  $0\nu\beta\beta$  signal. These backgrounds, already introduced earlier, are the  $2\nu\beta\beta$  of the source isotope, as well as disintegrations of  $^{208}\text{Tl}$  and  $^{214}\text{Bi}$ .

#### The $2\nu\beta\beta$ process

In the full energy range, the allowed  $2\nu\beta\beta$  decay stands as the dominant internal background type. Its total energy spectrum is a continuum, whose ending point stands around  $Q_{\beta\beta} = 2.99$  MeV, slightly increased by the detector's energy resolution. We simulated  $10^7$  events of this decay inside the source foils, in the full energy window. However, above a certain energy value, the number of  $2\nu\beta\beta$  events decreases very quickly. To offset this effect, we simulated additional  $10^7$  of this decay on a slightly lower energy range, that is to say above 2 MeV. The second set of simulations is normalised with the first one. In this way, we have the full energy spectrum of  $2\nu\beta\beta$  represented, even populated by events at higher energies.



### Source foils contamination by natural isotopes

As described in Sec. 3.2.1, after sources purification, remaining natural isotopes such as  $^{208}\text{Tl}$  or  $^{214}\text{Bi}$  can be present inside the foils. This class of contamination constitutes the principal internal source of background, with the  $2\nu\beta\beta$  decay. We simulated  $10^7$  decays both for the two isotopes, inside the source foils.

#### 6.1.2.2 Tracker contamination by natural isotopes

The presence of gaseous Radon-222 inside the tracker, mainly deposited on the copper wires, can produce events similar to internal one. In fact, one of the progeny of Radon-222, the Bismuth-214, can decay on (or near) a foil, and appear with a  $2e$  topology, becoming hard to distinguish from a double beta decay candidate. As this isotope is distributed throughout the whole tracking detection volume, to study the experiment's sensitivity, we simulated a large quantity of this decay on the tracker wires. This way, we maximise the amount of  $^{214}\text{Bi}$  events, coming from  $^{222}\text{Rn}$  decays, in the region of interest.

### 6.1.3 Outside detector backgrounds

This background category is populated by the external  $\gamma$ -ray flux produced by radioactive isotope decays in detector components or surrounding laboratory rocks, as well as neutron interactions in the shield. The most notorious difference is the fact that the SuperNEMO scintillator blocks are thicker than those of NEMO-3. Therefore, a gamma is more likely to be detected and rejected when crossing a scintillator. As a consequence, for the same PMTs radioactivity, the external gamma background rate is expected to be less important for the SuperNEMO demonstrator than for NEMO-3. Moreover, radiopurity measurements of SuperNEMO PMTs allow to conclude that their total activity is better than for those of NEMO-3, for the two principal considered isotopes  $^{208}\text{Tl}$  and  $^{214}\text{Bi}$  [14]. The NEMO-3 experiment set a limit on the external background number of counts, of  $< 0.2$  events in the  $2e$  topology, for the energy range [2.8;3.2] MeV (two electrons energy sum), for an exposure of 34.3 kg.y, with  $^{100}\text{Mo}$  sources [13]. Given the fact that SuperNEMO is expected to be better than NEMO-3 at rejecting external background events, we consider that all external backgrounds from outside the foil, apart from  $^{222}\text{Rn}$  in the tracking volume, are expected to be negligible, and were not simulated. Even if the regions of interest are slightly different between these two experiments, it produces negligible increase on the external background contribution.

In the following we present an optimisation of the event selection that has been set up to maximise the signal over background ratio in this specific topology.

## 6.2 Optimisation of event selection

The signature SuperNEMO is looking for is two electrons, emitted simultaneously from the same vertex on the source foils, with a two electrons energy sum compatible with  $Q_{\beta\beta} = 2.99$  MeV for the Selenium-82. Therefore, we conducted this analysis selecting only events matching the  $2e$  topology, where a reconstructed particle is tagged as an electron if it has

- a vertex on the source foils,
- a reconstructed track inside the wire chamber,
- and an associated calorimeter hit.

All these selections represent the so-called *first order cuts*.

Most of the double beta experiments are only sensitive to the total electron energy sum. SuperNEMO, by coupling both tracking and calorimetry technologies, is sensitive to individual energies and the angle between the two electrons. This feature confers the experiment the ability to individually characterise both electrons. By relying on these additional observables, *topological cuts* have been set up, in addition with the basic first order cuts described above. These topological cuts are designed to reject events where the two electrons are not emitted simultaneously, or from the same location on the source foils.

- The internal probability ( $P_{\text{int}}$ ), based on time-of-flight (TOF) computation, is detailed in Sec. 4.1.1. We chose to select events for which  $P_{\text{int}} > 4\%$ , insuring that non simultaneous events are rejected.



- The two reconstructed vertices on source foils should not be separated by more than 60 mm horizontally ( $\Delta y < 60$  mm), and by more than 70 mm vertically ( $\Delta z < 70$  mm), to maximise the selection of two electrons emitted at the same spot.



These cuts follow the NEMO-3 analysis on the background rejection, whose effectiveness were lately confirmed for the SuperNEMO demonstrator [15]. First order and topological cuts have efficiencies of selection differing for each type of decay. We computed these efficiencies, presented in Tab. 6.2. We observe

	First order cuts (%)	Internal probability (%)	Vertex distance (%)
$0\nu\beta\beta$	26.9	25.3	24.2
$2\nu\beta\beta$	9.16	8.57	8.01
$^{208}\text{Tl}$	0.106	0.0888	0.0821
$^{214}\text{Bi}$	0.168	0.151	0.140
$^{222}\text{Rn}$	0.0169	$7.3 \times 10^{-5}$	$4.27 \times 10^{-5}$

Table 6.2: Number of selected  $2e$  topologies compared with the total number of simulated decays, for first order cuts and topological cuts.

topological cuts allow the selection of a high proportion of  $0\nu\beta\beta$  signal events, while rejecting most of the background events, especially Radon decays inside the tracker.



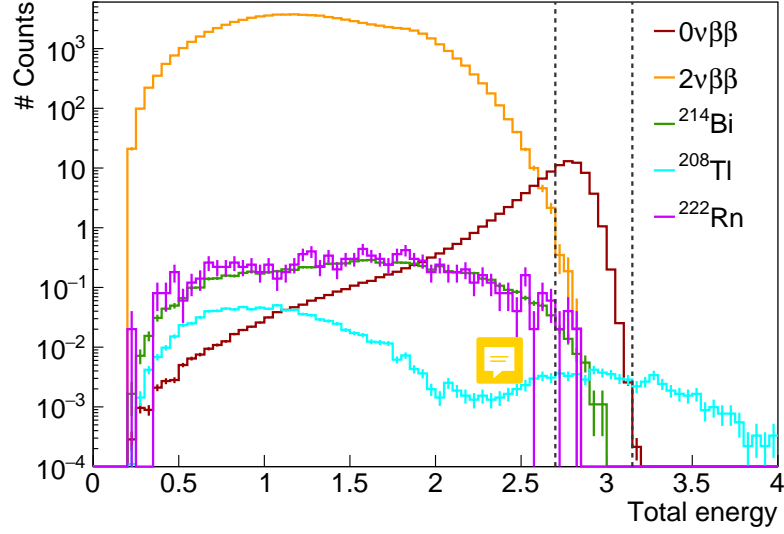
We present the total energy spectra for each simulated process, after event selection, in Fig. 6.1. The  $0\nu\beta\beta$  spectrum is peaked around 2.8 MeV, as the available energy  $Q_{\beta\beta} = 2.99$  MeV is degraded by electron energy losses before reaching the calorimeter (mainly inside the dense source material, as well as inside the wire chamber), explaining the asymmetric energy distribution. Given that Bismuth-214 is one of the progeny of Radon-222, their energy distributions follow the same variations. Moreover, as a great part of Radon-222 events have been rejected by topological cuts, they also both contribute at the same level in the full energy range. The  $^{208}\text{Tl}$  energy distribution reveals the internal conversion of the 2.6 MeV gamma, emitted after  $^{208}\text{Tl}$   $\beta^-$  disintegrations.



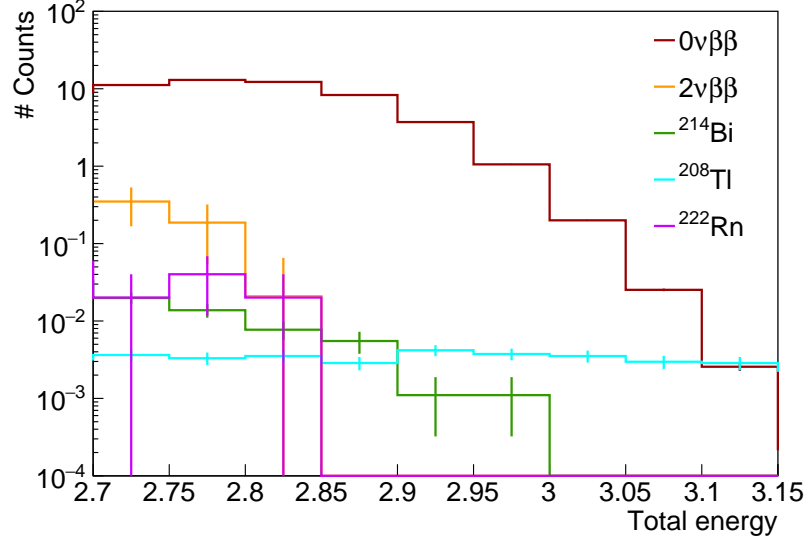
In the following section, we give informations about the expected number of background events, especially in the region of interest.

- dire aussi que là on présente pour Se avec champ. Du coup ya la coupure du premier ordre sur la courbure de la trace aussi.





(a)



(b)

Figure 6.1: Total energy spectra for the  $0\nu\beta\beta$  signal and main backgrounds, for (a) the full energy range, and (b) for the [2.7;3.2] MeV energy range, whose optimisation is discussed in Sec. 6.3.

### 6.3 Expected number of background events and optimisation of the region of interest

As the two electrons energy sum for the  $0\nu\beta\beta$  is expected as a peak (enlarged by electron energy losses and calorimeter energy resolution), it is interesting to constrain the  $0\nu\beta\beta$  decay searches to a given energy range, the so-called *region of interest* (ROI). In the following, we expose how the search for the best limit on  $T_{1/2}^{0\nu}$  is a guide to determine the best ROI.

For a given energy range, the expected upper limit of the  $0\nu\beta\beta$  half-life depends

### 6.3. Expected number of background events and optimisation of the region of interest

on the characteristics of the detector. First, it depends on the signal detection efficiency  $\epsilon_{0\nu}$  in this energy window, secondly on the source isotope nature, as well as the detector's exposure  $m \times t$ . It follows

$$T_{1/2}^{0\nu} > \frac{\mathcal{N}_A \log 2}{M} \times \frac{\epsilon_{0\nu} \times m \times t}{N_{0\nu}^{\text{exclus}}}, \quad (6.1)$$

with  $\mathcal{N}_A$  the Avogadro number,  $m$  the quantity of isotope in the source foils,  $M$  its molar mass, and  $t$  the total time of data taking.  $N_{0\nu}^{\text{exclus}}$  is the number of signal events excluded, calculated with the Feldman-Cousins statistics from the total expected number of background events, for a given confidence interval. The Feldman-Cousins statistics [16] is a wide-used method in rare events search experiments, providing confidence intervals for upper limits in the case of Poisson processes with background. Given the expected number of background events, this method gives a limit on the number of expected signal events  $N_{0\nu}^{\text{exclus}}$ . As a consequence, the limit on  $T_{1/2}^{0\nu}$  described in Eq. (6.1) is provided as a function of the energy range  $[E_{\min}; E_{\max}]$ . The region of interest holds for the search of  $0\nu\beta\beta$  decay is the one that maximises the limit on  $T_{1/2}^{0\nu}$ . It depends on the exposure, on the isotope chosen for the experiment, as well as its total quantity inside the source foils, all of these different conditions being detailed in the following. To give an order of magnitude, we found that, for the demonstrator exposure, with  $^{82}\text{Se}$  sources, and a 25 G magnetic field, the best ROI is [2.7;3.15] MeV.

Therefore, in order to evaluate  $N_{0\nu}^{\text{exclus}}$ , and later the demonstrator's sensitivity to the  $0\nu\beta\beta$  decay, we must determine the number of background events occurring in the region of interest. This calculation, depends on the background.

- The  $2\nu\beta\beta$  background

In Eq. (6.1), we defined the upper limit on  $T_{1/2}^{0\nu}$  from the number of excluded signal events, and the signal selection efficiency  $\epsilon_{0\nu}$ . The same way, we can define the number of observed  $2\nu\beta\beta$  events  $N_{2\nu}$  from the half-life  $T_{1/2}^{2\nu}$  and the  $2\nu\beta\beta$  selection efficiency  $\epsilon_{2\nu}$ ,

$$N_{2\nu} = \frac{\mathcal{N}_A \log 2}{M} \times \frac{\epsilon_{2\nu} \times m \times t}{T_{1/2}^{2\nu}}. \quad (6.2)$$

- Natural radioactive backgrounds

Considering the background activities  $A_{\text{rad.}}$ , and  $\epsilon_{\text{rad.}}$  their selection efficiencies in a given energy window, the number of background events is given as

$$N_{\text{rad.}} = A_{\text{rad.}} \epsilon_{\text{rad.}} \times m \times t \quad (6.3)$$

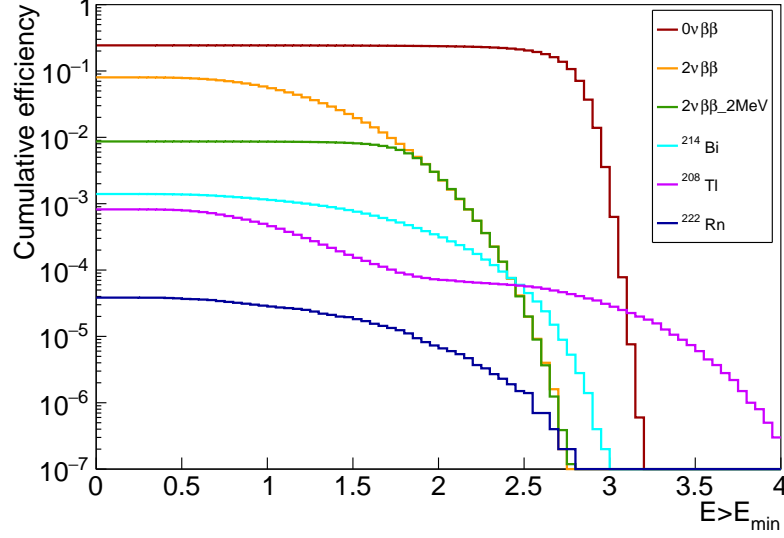
for the  $^{208}\text{Tl}$  and  $^{214}\text{Bi}$  internal background, and as

$$N_{\text{rad.}} = A_{\text{rad.}} \epsilon_{\text{rad.}} \times V \times t, \quad (6.4)$$

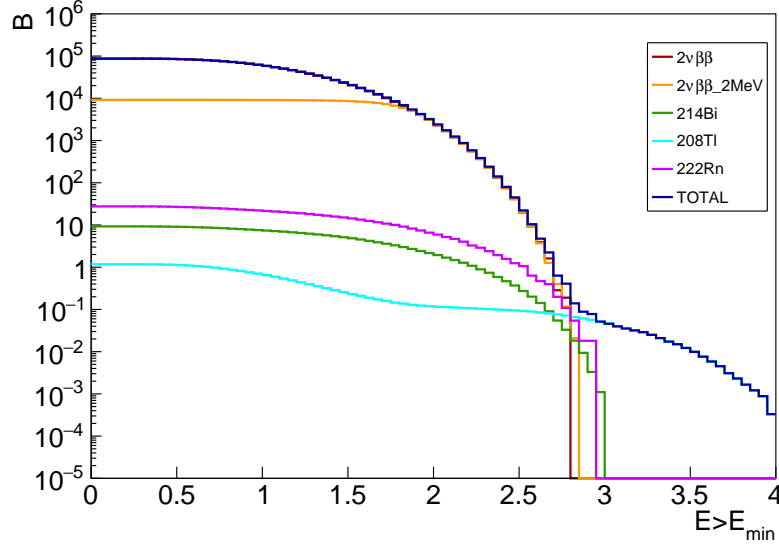
for the  $^{222}\text{Rn}$  background, with  $V = 15.3 \text{ m}^3$  the tracker volume.

For Eqs. (6.1) to (6.4), we need to evaluate the event selection efficiencies, for given energy windows, in order to set the best limit on the  $0\nu\beta\beta$  decay half-life. These

efficiencies are obtained by comparing the number of selected events to the number of Monte-Carlo events, for each process. We choose to compute these efficiencies in  $E > E_{\min}$  energy ranges, to . The cumulative efficiency spectra are presented in Fig. 6.2a. Once computed, the efficiency of selection helps finding the number of background events expected, displayed in Fig. 6.2b.



(a)



(b)

Figure 6.2: (a) Efficiency spectra for  $E > E_{\min}$ , for the  $0\nu\beta\beta$  signal and for the main backgrounds. (b) Expected number of background events, for  $E > E_{\min}$ .

Thereafter, we present and discuss the results obtained in the framework of this study, regarding different exposures (demonstrator and final detector), and different internal background activities (presented in Tab. 6.3). Also, and this is

the main purpose of this study, we discuss the influence of the presence of the magnetic field on the final detector's sensitivity.

## 6.4 The 25 Gauss magnetic field

As detailed in Sec. 6.4, the SuperNEMO demonstrator was originally designed with a copper coil, similarly to NEMO-3, delivering a magnetic field inside the tracker volume, aiming to provide an electron/positron discrimination by fitting the curved particle tracks by an helix. Studies have been lead to evaluate its influence on the optical modules and on the event reconstruction [8][17].

### 6.4.1 Influence of the magnetic field on optical modules and reconstruction efficiency

SuperNEMO PMTs are protected from the external magnetic field by an iron shield. Unfortunately, the latter do not perfectly protect the PMTs, and a residual magnetic field is measured inside the shieldings, leading to charge losses and worsened energy resolution. It was shown that applying a 25 G magnetic field, and protect the PMTs with iron magnetic shields would be optimal, but not without consequences. In fact, for the recommended value of 25 G for the magnetic field, PMT charge losses would be close to 8%, and the PMT energy resolution would be increased of  $\sim 3\%$ . Moreover, the PMTs shieldings could themselves severely impact the shape of the field lines, as well as its strength: with a 25 G magnetic field generated by the copper coil, barely 10 G is expected near the source foils, and this value decreases quickly as we get closer to the calorimeter walls. The reconstruction efficiency could therefore be greatly impacted: the magnetic field intensity varying from the source foils to the calorimeter wall, electrons trajectory curvatures are not constant, and the track is less well fitted. This effect is higher as the electron energy decreases.

Despite the fact that magnetic shields were designed and installed to protect the PMTs, this field can have a great impact on the calorimeter detection efficiency, and thus could degrade the detector's sensitivity to the  $0\nu\beta\beta$  decay. If the studies cited have evaluated the influence of the presence of the magnetic field on the reconstruction efficiency of  $0\nu\beta\beta$  events, it remains to be seen its consequences on the final demonstrator sensitivity.

### 6.4.2 Simulations of the magnetic field inside the demonstrator and reconstructed track fit

In order to study the influence of the magnetic field on the Selenium-82  $0\nu\beta\beta$  sensitivity, the simulations and reconstructions of decays described in Sec. 6.1 have been performed in three different conditions:

- simulations where the magnetic field is turned off,

- simulations with a 25 G *uniform* magnetic field (following recommendations [8]),
- simulations with a 25 G *mapped* magnetic field, taking into account more realistic variations of the magnetic field inside the detector [18].

Each magnetic field conditions have the same number of simulated events, as summed up in Tab. 6.1. Depending on the case considered, the electrons will not have the same trajectory curvature: in the first no-field case, electron tracks are straight lines. The fitting algorithm have thus be modified to match line trajectories. In the second uniform-field case, the best track fit is performed by helices. Finally, the best tracking option (line or helix) for the third mapped-field will be discussed in the next section.

## 6.5 Demonstrator sensitivity to the $0\nu\beta\beta$ decay

The limit set on the  $T_{1/2}^{0\nu}$ , given by Eq. (6.1), depends on the background level. One of the main goal of this study is also to determine the dependence of the sensitivity on the magnetic field applied inside de wire chamber. In the following, we detail the results presented in Fig. 6.3, looking at one after another the influence of the contamination levels and the magnetic field on the sensitivity to the  $0\nu\beta\beta$  decay.

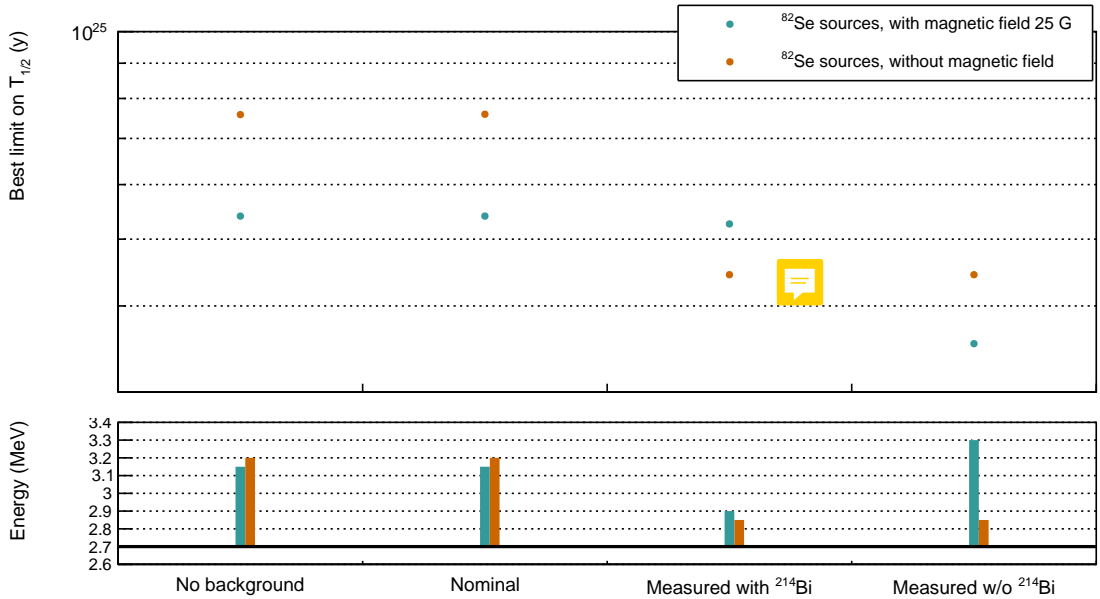


Figure 6.3: Best limit set on  $0\nu\beta\beta$  half-life (top pad), and the corresponding energy (bottom pad), as a function of the contamination level considered.

This study was conducted jointly with the PhD student Axel Pin, from CENBG. Although we both worked on the whole of the analysis, I have here to present in detail the results regarding the influence of the magnetic field, while Axel Pin will present in detail the possibility of changing the Selenium sources by Neodymium [19]. Sec. 6.7 will, however, briefly present the results of the Neodymium analysis.



### 6.5.1 Influence of the contamination levels

Targeted levels of contaminations inside the source foils and inside the wire chamber have been set to match the expectations on final detector's sensitivity to the  $0\nu\beta\beta$ . After sources production, preliminary measurements have been performed to determine the actual  $^{208}\text{Tl}$  and  $^{214}\text{Bi}$  contamination levels. Both these values are presented in Tab. 6.3. We notice the measured contamination

	Nominal activities	Measured activities
$^{208}\text{Tl}$	$10 \mu\text{Bq.kg}^{-1}$	$54 \mu\text{Bq.kg}^{-1}$
$^{214}\text{Bi}$	$2 \mu\text{Bq.kg}^{-1}$	$< 290 \mu\text{Bq.kg}^{-1}$
$^{222}\text{Rn}$	$0.15 \text{ mBq.m}^{-3}$	$0.15 \pm 0.02 \text{ mBq.m}^{-3}$ [12]

Table 6.3: Real and targeted nominal activities for the SuperNEMO detector.

levels are higher than expected. This is partly explained by new source production techniques (Sec. 3.2). We give in this section its consequences on the demonstrator's sensitivity to the  $0\nu\beta\beta$  decay.

In Fig. 6.3, four distinct levels of internal contaminations are considered:

- the *no background* case, a hypothetical case where the source foils and the tracker are non contaminated at all,
- the *nominal* case, where the targeted level of contaminations are considered,
- the two *measured* cases (*with* and *without*  $^{214}\text{Bi}$ ), that take into account the measured levels of contaminations. As the  $^{214}\text{Bi}$  activity is provided by BiPo measurements as an upper limit, it is possible for this level to be lower than  $290 \mu\text{Bq/kg}$ . So we present the results both considering a zero or  $290 \mu\text{Bq/kg}$  for the internal Bismuth-214.

Let us first compare the two firsts, where no difference between the best  $T_{1/2}^{0\nu}$ , nor between the region of interests, is observed. This is explained by the Feldman-Cousins statistics employed to determine the number of expected signal events, given the number of observed background events. When the expected number of background events is negligible (which is the case here), the probability  $p$  to observe  $n_s$  events, expecting  $s$  signal events is given by a Poisson distribution

$$p = \frac{e^{-s} s^{n_s}}{n_s!}. \quad (6.5)$$

If no background event is observed - and this is assumed to put an upper half-life limit - then  $p = e^{-s}$ . We can set an upper limit on the expected signal yield  $s$  excluding values of  $s$  for which  $p < \alpha$ , here considering  $\alpha = 10\%$  ( $1 - \alpha = 90\%$  CL). The upper limit for a negligible expected number of background and no signal events observed is therefore  $s \leq 2.303$  (90% CL). A direct consequence is, considering that the background levels for the two first cases are negligible, they both reach this limit on the expected number of signal events.

We focus now on the two last contamination cases, for which the measured natural isotope activities are used to determine the best limit on  $T_{1/2}^{0\nu}$ . For the case where we consider the foils are non contaminated by the  $^{214}\text{Bi}$  isotope, only a slight decrease in sensitivity is observed, compared with the ideal no background case [à revoir avec ajout du Radon qui devrait affecter la demie-vie]. If we now apply the  $290\text{ }\mu\text{Bq/kg}$  upper limit, the level of total internal contaminations is no more negligible, and influence greatly the value of  $T_{1/2}^{0\nu}$ , decreasing the experiment's sensitivity by a factor 1.5.

After looking at the effect of contaminations on the sensitivity, we review the influence of the magnetic field inside the detector.

### 6.5.2 Influence of the magnetic field

As described in Sec. 6.4, the presence of a magnetic field of 25 G could influence the optical modules performances. In the simulated detector, such effects are not yet implemented, therefore can't be observed in the framework of this analysis. However, possible degradation of the event reconstruction efficiency.

We oppose in Fig. 6.3 the  $T_{1/2}^{0\nu}$  results with and without this field inside the detector. A third result is also presented, with the mapped field.

- avec variation coupure énergie
- Parler du champ non uniforme/attenuation

## 6.6 Final detector sensitivity

The final goal of the SuperNEMO demonstrator is to demonstrate that the NEMO technology is scalable to reach high half-life sensitivity on the  $0\nu\beta\beta$  decay. It was therefore mandatory to study the case of the final detector sensitivity, consisting in building 20 modules similar to the SuperNEMO demonstrator, to reach unprecedented levels on effective neutrino masses.

## 6.7 Other isotopes

In the case SuperNEMO demonstrate the feasibility of a large-scale tracko-calo experiment, we would examine the possibility of different source isotopes, as done on NEMO-3. In this framework, we present here the sensitivity of SuperNEMO to the  $0\nu\beta\beta$  of Neodymium-150. The  $^{150}\text{Nd}$  has a more favorable  $Q_{\beta\beta}$  than  $^{82}\text{Se}$ , with  $Q_{\beta\beta} = \text{MeV}$ , . However, its  $T_{1/2}^{2\nu}$  is lower, with  $9.1 \times 10^{18}$  years [ref]. For this study, we keep the  $^{82}\text{Se}$  values for the contaminations, despite different purification efficiencies for the two isotopes.

distribution  $t_{1/2}$  avec différents échantillons de simus (17.5 kg.y)

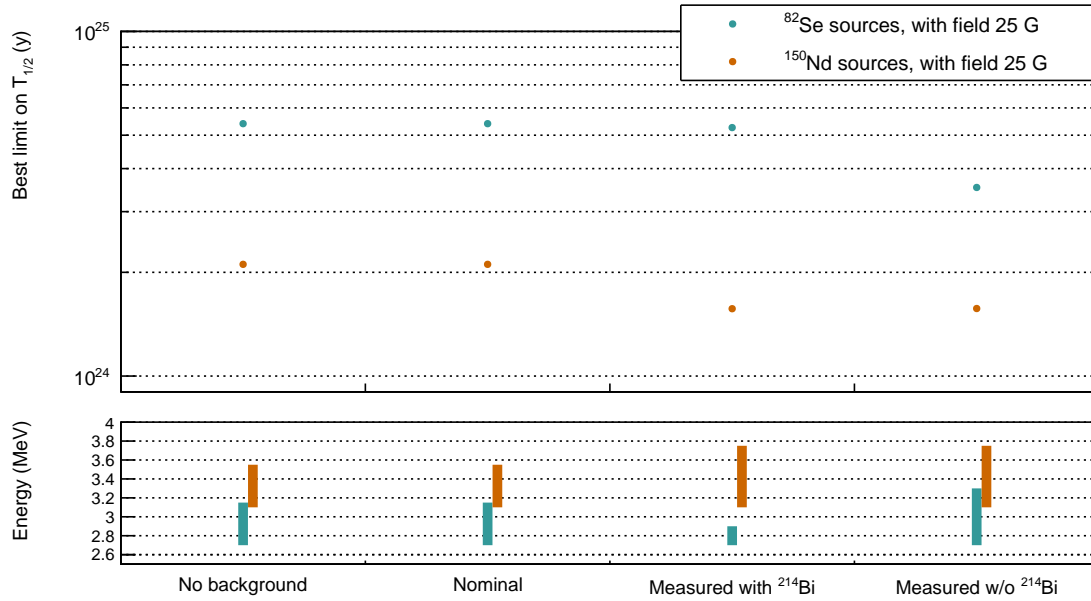


Figure 6.4: Best limit set on  $0\nu\beta\beta$  half-life (top pad), and the corresponding ROI (bottom pad), as a function of the contamination level considered, considering  $^{150}\text{Nd}$  sources and an exposure of 17.5 kg.

## 6.8 Conclusion

- Etude plus générale avec bkg externe+lab (reprendre chiffres NEMO3) + neutrons (cf NEMO3)
- Plot général récap tous résultats
- delayed cells- $\gamma$ improvement, cf NEMO 3
- ouverture sur possibilité d'étudier l'influence de la résolution en temps des PMs sur l'eff des coupures (Pint)
- cellules tracker dead- $\gamma$  refaire analyse
- manque de stat pour le neodyme car ROI haute E
- légères diff avec résultats axel car légères diff dans sélections d'év car utilisation PID
- tenir compte de la dégradation en énergie dans les simus du au B



---

## Bibliography

- [1] M. et al. Agostini. Probing majorana neutrinos with double- $\beta$  decay. *Science* 365, 1445, 2019.
- [2] S.I. et al Alvis. Search for neutrinoless double-beta decay in  $^{76}\text{Ge}$  with 26 kg-yr of exposure from the majorana demonstrator. *Phys. Rev. C*, 100, 2019.
- [3] O. et al. Azzolini. First result on the neutrinoless double- $\beta$  decay of  $^{82}\text{Se}$  with cupid-0. *Phys. Rev. Lett.*, 120:232502, Jun 2018.
- [4] C. et al. Alduino. First results from cuore: A search for lepton number violation via  $0\nu\beta\beta$  decay of  $^{130}\text{Te}$ . *Phys. Rev. Lett.*, 120:132501, Mar 2018.
- [5] J. B. et al. Albert. Search for neutrinoless double-beta decay with the upgraded exo-200 detector. *Phys. Rev. Lett.*, 120:072701, Feb 2018.
- [6] A. et al. Gando. Search for majorana neutrinos near the inverted mass hierarchy region with kamland-zen. *Phys. Rev. Lett.*, 117:082503, Aug 2016.
- [7] R. et al. Arnold. Probing new physics models of neutrinoless double beta decay with supernemo. *Eur. Phys. J. C*, 2010.
- [8] S. Clavez. *Development of reconstruction tools and sensitivity of the SuperNEMO demonstrator*. PhD thesis, Université Paris Sud, 2017.
- [9] R. et al. Arnold. Final results on  $^{82}\text{Se}$  double beta decay to the ground state of  $^{82}\text{Kr}$  from the nemo-3 experiment. *Eur. Phys. J. C*, 2018.
- [10] Tretyak V.I. Ponkratenko O.A. and Zdesenko Yu.G. The event generator decay4 for simulation of doublebeta processes and decay of radioactive nuclei. *Phys. At. Nucl.*, 63:1282–1287, Jul 2000.
- [11] Gomez-Cadenas et al. Physics case of supernemo with  $^{82}\text{Se}$  source. Internal presentation, 2008.
- [12] Xin Ran Liu. Radon mitigation strategy and results for the supernemo experiment. IoP APP / HEPP Conference, 2018.

- [13] R. et al. Arnold. Results of the search for neutrinoless double- $\beta$  decay in  $^{100}\text{mo}$  with the nemo-3 experiment. *Phys. Rev. D*, 2015.
- [14] Perrot F. Radiopurity measurements for 8" pmts and preliminary budget for the sn demonstrator. Internal presentation, 2017.
- [15] Steven Calvez. Updates on the demonstrator sensitivity and radon study. Internal presentation, 2014.
- [16] Cousins D. Feldman G. A unified approach to the classical statistical analysis of small signals. *Phys.Rev.*, pages 3873–3889, 1999.
- [17] Garrido X. Bongrand M. Hamamatsu 8" pmt test in magnetic shield. Internal presentation, 2014.
- [18] Snow S. A magnetic field map for the tracker. Internal presentation, 2015.
- [19] A. Pin. *Recherche de la nature du neutrino via la décroissance double bêta sans émission de neutrinos. Caractérisation et optimisation du calorimètre SuperNEMO et impact sur la recherche de la décroissance du  $^{82}\text{Se}$* . Développement du premier prototype LiquidO. PhD thesis, Université Bordeaux-Gradignan, 2020.
- [20] Nucleid database.